Journal of Colloid and Interface Science 581 (2021) 251–261

Contents lists available at ScienceDirect

Journal of Colloid and Interface Science

journal homepage: www.elsevier.com/locate/jcis

Regular Article

Self-assembled nanoparticle-coated interfaces: Capillary pressure, shell formation and buckling

Q. Liu [a,*,1], Z. Sun [b,1], J. Carlos Santamarina [a,1]

[a] Earth Science and Engineering, King Abdullah University of Science and Technology (KAUST), Thuwal 23955-6900, Saudi Arabia
[b] Hildebrand Department of Petroleum and Geosystems Engineering, The University of Texas at Austin, Austin, TX, United States

GRAPHICAL ABSTRACT

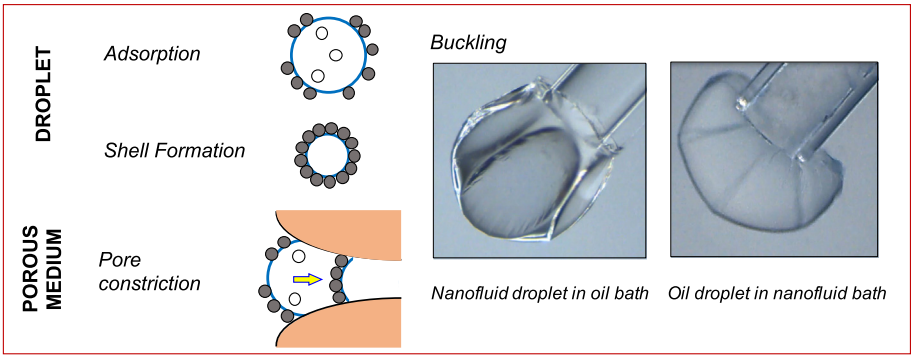

ARTICLE INFO

Article history:
Received 22 March 2020
Revised 22 July 2020
Accepted 22 July 2020
Available online 27 July 2020

Keywords:
Particle-coated interface
Buckling patterns
Multi-phase flow
Capillarity
Oil displacement

ABSTRACT

Hypothesis: Particle accumulation at liquid-liquid or liquid-gas interfaces can significantly alter capillary behavior and give rise to unusual interfacial phenomena including the asymmetric macroscopic mechanical response of the interface.

Experiments: This study explores the accumulation of cetyltrimethylammonium bromide-modified nanoparticles at fluid interfaces and the subsequent mechanical response of nanoparticle-coated droplets during contraction and expansion. Droplet tests involve the simultaneous recording of the droplet shape and the capillary pressure. Complementary single-pore experiments examine the response of particle-coated interfaces as they traverse a pore constriction.

Findings: Interfaces promote order. The time-dependent nanoparticle accumulation at the interface is diffusion-controlled. The nanoparticle coated droplets can sustain negative capillary pressure before they buckle. Buckling patterns strongly depend on the boundary conditions: non-slip boundary conditions lead to crumples while slip boundary conditions result in just a few depressions. The particle-coated interface exhibits asymmetric behavior in response to particle-level capillary forces: an "oil droplet in a nanofluid bath" withstands a significantly higher capillary pressure difference than a "nanofluid droplet in an oil bath". A first-order equilibrium analysis of interaction forces explains the asymmetric response. Single-constriction experiments show that the formation of particle-coated interfaces has a pronounced effect on fluid displacement in porous media.

* Corresponding author.
E-mail address: qi.liu@kaust.edu.sa (Q. Liu).
[1] Authors have contributed equally.

https://doi.org/10.1016/j.jcis.2020.07.110
0021-9797/

Nomenclature

a	Particle radius (m)
c	Surface coverage of particles []: c_0 initial, c_L at jamming, c_D at dense packing state
E	Interfacial free energy (J)
F	Inter-particle force (N)
F_c	Capillary force (N)
H	Particle-particle distance (m)
N	Number of particles along droplet perimeter []
N_0	The total number of particles at the interface []
P	Fluid pressure (Pa)
R	The radius of the droplet (m): R_0 initial, R_L at jamming, R_D at dense packing state
t_{ad}	Adsorption time (hr)
α	Bending angle (°)
β	Packing factor []
γ	Interfacial tension (mN/m): γ_{ow} oil-water, γ_A apparent
ΔP	Capillary pressure (Pa)
ζ	Zeta potential (mV)
θ	Contact angle (°):θ_A advancing, θ_R receding
κ	Curvature (m^{-1})
μ	Dynamic viscosity (mPa·s)
ϕ	Polar angle (°)

1. Introduction

Particle accumulation at a liquid/liquid or liquid/gas interface may confer distinctive properties to the interface and support unique applications such as the stabilization of emulsions and foams i.e., Pickering emulsion [1,2], enhanced oil recovery [3], drug delivery [4], or augmented sealing capacity for geological CO_2 storage [5]. The properties of the particle-coated interface evolve during the contraction of the interface. Overall, the interface exhibits a viscoelastic response at small strains and strain rates [6,7] as observed in interfacial rheology measurements [6,8]. Consequently, some deformation analyses have considered the interface as an elastic sheet [9–11]. However, elastic models ignore the granular nature of the particle raft, overlook the complexity of particle-interface interactions [12–15], and fail to capture evolving phenomena during contraction and expansion, such as buckling [16], particle expulsion [16–18], and the formation of multilayers [17,19].

Previous experimental studies characterized the deformation of the particle-coated interface using Langmuir-Blodgett troughs and Wilhelmy plates to determine the evolving surface pressure while decreasing the surface area [20–22]. Reported results show that the surface stress is nonuniform, probably due to the granular nature of the particle-coated interface and the large surface area of Langmuir troughs [10,23,24].

Furthermore, the flat interface in trough experiments differs from mixed-fluid conditions in porous media where interfaces are small and inherently curved. The capillary pressure ΔP across a curved interface depends on the interfacial tension γ and the mean curvature κ as predicted by the Young-Laplace equation: $\Delta P = 2\gamma\kappa$. Capillary phenomena dominate fluid displacement patterns in porous media [25,26], determine residual saturations [27,28] and give rise to pore-scale instabilities such as Haines jump [29,30] and snap-offs [31,32]. The contraction and expansion of droplets resemble the evolution of fluid interfaces as they traverse a porous medium where they experience sequentially converging and diverging cross-sections. However, only a few studies have investigated the deformation of particle-coated bubbles or droplets [33–35], and changes in capillary pressure caused by particle-coated interfaces remain unclear.

This study explores the mechanical response of nanoparticle-coated droplets during contraction and expansion. We measure the capillary pressure, explore the asymmetric buckling behavior of nanoparticle-coated interfaces, and investigate implications on multi-phase flow in porous media.

2. Experimental study

2.1. Setup for droplet studies

The experimental setup resembles the microtensiometer used for measuring capillary pressure, interfacial tension and interfacial rheology [34,36,37], and consists of a precision syringe pump, a high-resolution pressure transducer, and a glass capillary immersed in a liquid bath (Fig. 1a). Experiments use borosilicate glass capillaries (Drummond Scientific Company, ID = 0.56 mm and OD = 0.79 mm). We covalently graft perfluorodecyltrichlorosilane (FDTS) through molecular vapor deposition for tests that require hydrophobic capillaries (MVD100E, AMST). The advancing θ_A and receding θ_R contact angles on the hydrophobic FDTS-coated glass surfaces are θ_A = 105° ± 1° and θ_R = 72° ± 1° (2 μL deionized water drops dispensed/retracted at 0.2 $\mu L \cdot s^{-1}$).

Tests involve a nanofluid (described below) and mineral oil (Mineral oil light, Sigma-Aldrich; density ρ = 877 kg/m^3, dynamic viscosity μ = 21 mPa·s and oil–water interfacial tension γ_{ow} = 34.2 mN/m). Experiments start by filling the bath with either fluid; then the syringe pump (Braintree Scientific, Inc., BS-8000) delivers the other fluid to the tip of the glass capillary to create a droplet of the desired volume. The droplet rests for a preset adsorption time t_{ad} to allow nanoparticles to diffuse and self-assemble at the interface. Then, we reduce the droplet volume by withdrawing the fluid at a low flow rate (q = 0.2 ml/hr) to ensure that the nanofilm is in a quasi-static condition during contraction. A microscope (Stemi 2000-CS, ZEISS) records the droplet deformation and the pressure transducer (PX40, OMEGA) measures the capillary pressure throughout the droplet expansion and contraction stages. The pressure difference due to viscous loss between the pressure transducer and the oil–water interface is in the order of 1 Pa for the flow rate used in these experiments, and it is much smaller than the range of the measurements (>100 Pa). We calibrate the pressure transducer using hydrostatic pressure to remove any offset caused by trapped air. There are no dynamic instabilities in our experiments, therefore, the system compliance does not affect pressure measurements [29,38,39].

2.2. Nanofluids: concentration optimization

Our experiments involve silica nanoparticles (Sigma-Aldrich; size d = 88 nm from dynamic light scattering – Zetasizer ZS). We modify the nanoparticle surface with the cationic surfactant cetyltrimethylammonium bromide CTAB (Sigma-Aldrich, purity

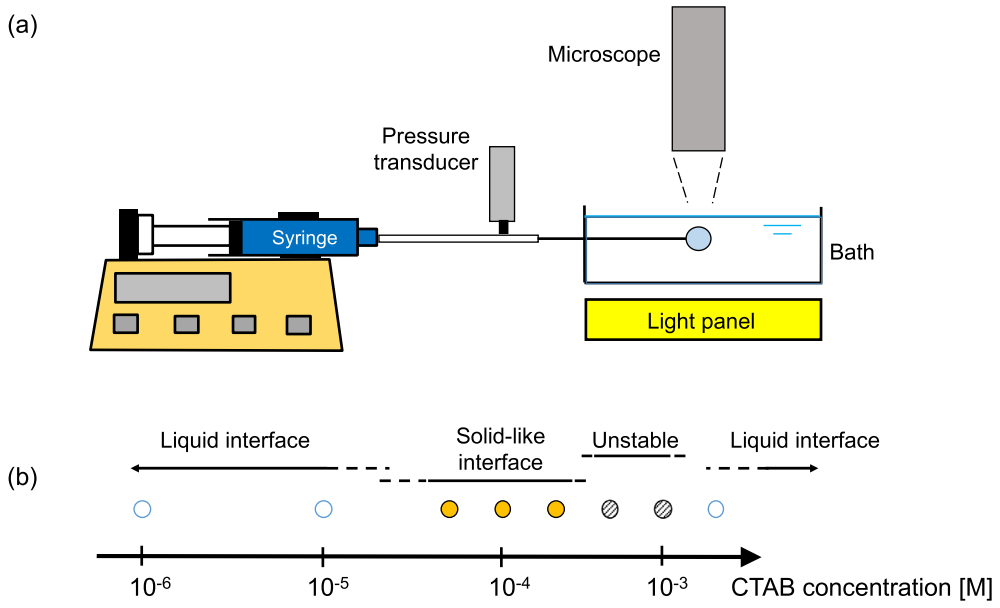

Fig. 1. Experimental study. (a) Configuration. (b) Preliminary droplet tests for the optimization of CTAB concentration.

>99%). The preparation of the nanofluids starts by mixing nanoparticles with the CTAB solution at a solids fraction of 5 g/L, followed by sonication for 40 min. We vary the CTAB concentration from 10^{-6}M to 2×10^{-3}M. Nanoparticles are negatively charged (zeta potential $\zeta = -60$ mV, measured by Zetasizer Nano ZS, Malvern Instruments), therefore, CTAB adsorption to the silica nanoparticles prevails and the surfactant is almost completely removed from the bulk aqueous phase. The interfacial tension measured for the supernatant water after centrifugation is indistinguishable from the deionized water interfacial tension (see also [40]).

Preliminary droplet contraction experiments show that: (1) the interface behaves as a liquid-liquid interface when the concentration of CTAB is less than 10^{-5}M; (2) granular jamming and shell-like interfaces develop when the concentration of CTAB is between 10^{-5}M and 2×10^{-4}M; and (3) the nanofluid becomes unstable at higher CTAB concentrations (Fig. 1b). Furthermore, there is evidence that NaCl and NaOH promote the adsorption of surfactants and increase the stability of nanofluids [41]. Consequently, the engineered nanofluid used in all tests reported in this article consists of 5 g/L silica nanoparticles, 8×10^{-5}M CTAB, 1 mM NaCl, and has a pH = 10 (adjusted by NaOH).

3. Results

We tested two different scenarios: (a) the contraction of a "*nanofluid droplet in an oil bath*" and (b) the contraction of an "*oil droplet in a nanofluid bath*". In both cases, we used FDTS-coated capillary tubes and allowed t_{ad} = 10 min for adsorption. The following results highlight salient features of particle-coated interfaces observed in multiple repeatable experiments.

3.1. Contraction of a nanofluid droplet in an oil bath

Fig. 2a presents the measured capillary pressure and concurrent microphotographs gathered during the contraction of a nanofluid droplet in oil (See Supplementary Material V1 for the complete video). The contraction process displays four distinct stages (the numbered red markers refer to the sequence of microscope images shown below each plot).

Stage A (images 1 and 2): the droplet remains spherical and the measured capillary pressure $\Delta P = P_{nanofluid}\text{-}P_{oil}$ decreases slowly. For comparison, the capillary pressure for a water droplet in oil - without nanoparticles-increases as the droplet size decreases in agreement with Laplace's equation $\Delta P = 2\gamma_{ow}/R$ (refer to the dashed line on Fig. 2a – experimental measurements in Supplementary Material S1). The initial interfacial tension is γ_A = 34.2 mN/m at Point 1 (evaluated using the Laplace equation). Then the apparent interfacial tension gradually decreases as the droplet contracts during Stage 1.

Stage B (images 2 and 3): while the droplet remains spherical, the capillary pressure decreases rapidly towards $\Delta P \rightarrow 0$ during this stage. Apparently, repulsive particle–particle interactions reduce the apparent interfacial tension to minimal values $\gamma_A \rightarrow 0$.

Stage C (images 3 to 5): a distinct shell-like response emerges and the particle-coated interface begins to wrinkle. The capillary pressure remains constant and very low ΔP = 10 Pa as the droplet contraction continues.

Stage D (image 5): the capillary pressure decreases below zero and the film folds into the capillary tube.

3.2. Contraction of an oil droplet in a nanofluid bath

The response of an "oil droplet in a nanofluid bath" is strikingly different from the case of the "nanofluid droplet in an oil bath" shown above. There are three salient stages in this case (Fig. 2b – see Supplementary Material V2 for a complete video).

Stage A (before image 1): the droplet remains spherical as it contracts at a constant pressure.

Stage B (images 1 to 4): the pressure decreases monotonically while the droplet contracts with convex shapes. Eventually a granular shell forms. The stiff shell contracts past the tube edge and a few localized wrinkles initiate around the tube edge (images 3 and 4). The capillary pressure $\Delta P = P_{oil}\text{-}P_{nanofluid}$ decreases below zero and the granular shell resists contraction; in fact, the particle-coated interface sustains a significant negative pressure difference $\Delta P = -100$ Pa.

Stage C (images 4 and 5): finally, the particle-coated interface experiences a sudden collapse and the shell loses its ability to resist the large pressure difference ΔP (image 5). Changes between images 4 and 5 suggest a pronounced re-structuring of the

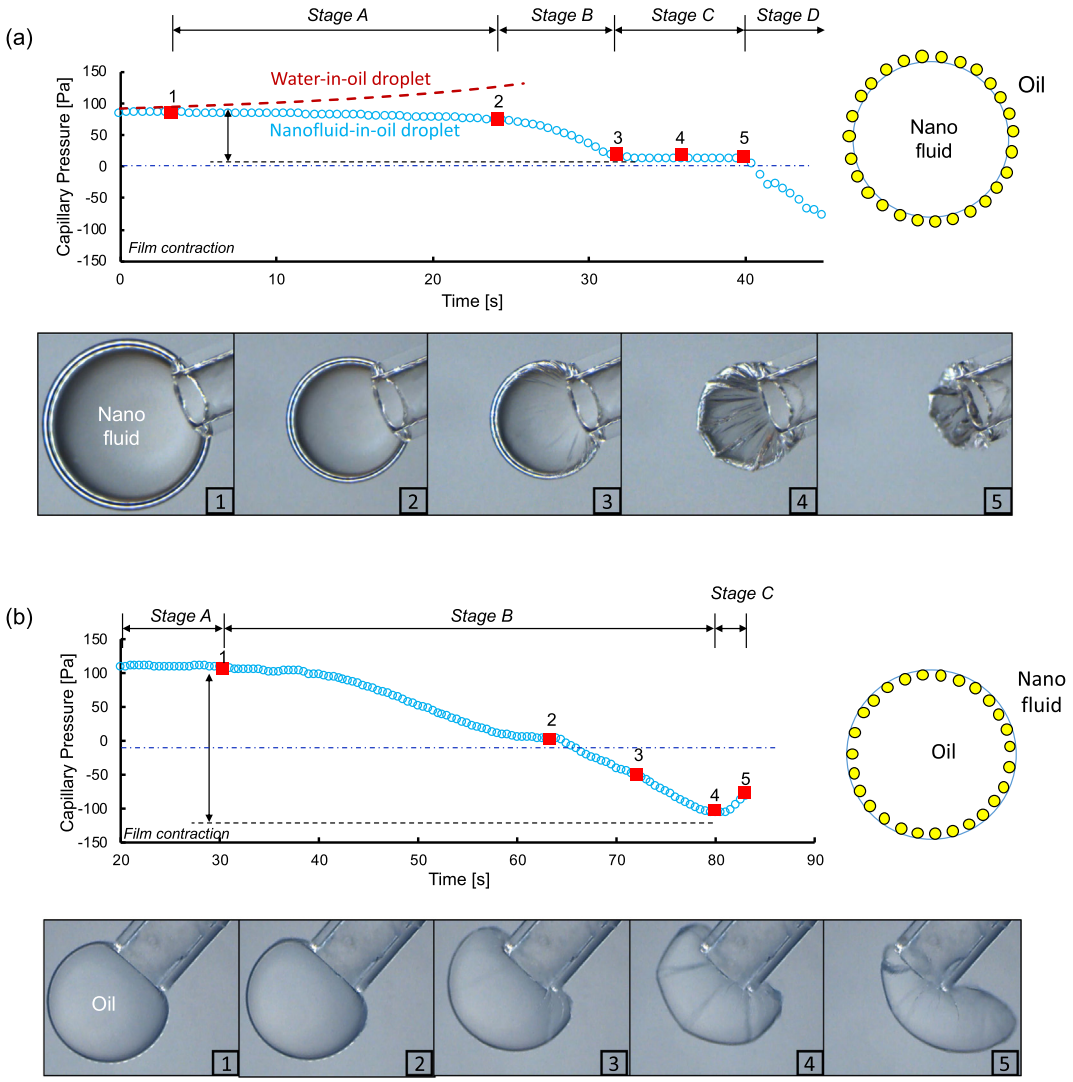

Fig. 2. Droplet contraction experiments at constant extraction flow rate q = 0.2 ml/hr. (a) Contraction of a nanofluid droplet in an oil bath. (b) Contraction of an oil droplet in a nanofluid bath. Note: adsorption time t_{ad} = 10 mins, FDTS coated capillary tube, ID = 0.56 mm and OD = 0.79 mm. The numbered red markers refer to the sequence of microscope images shown below each plot. (For interpretation of the references to colour in this figure legend, the reader is referred to the web version of this article.)

nanoparticle assembly at the interface as early localized wrinkles vanish after the shell collapses.

3.3. Effect of boundary wall wettability on the buckling pattern

Buckling patterns appear to be affected by the boundary conditions against the capillary wall. We tested this observation by comparing contraction experiments for a "*nanofluid droplet in an oil bath*" using both FDTS-coated glass capillaries and hydrophilic uncoated glass capillaries (Note: all other experimental parameters are identical). Multiple experimental observations show that hydrophobic FDTS coated glass capillaries always produce crumpling patterns (multiple folds, Fig. 3a – Supplementary Material V1) while hydrophilic glass capillaries trigger buckling patterns (a few folds, Fig. 3b – Supplementary Material V3). Apparently, the hydrophobic interaction between the FDTS-coated glass and the CTAB-modified silica particles generates a "pinned joint" which constrains the displacement between the particles at the interface and the glass capillary [42]. On the other hand, the untreated glass capillaries lead to a "roller joint" so that particles at the interface displace along the glass edge and only a few large folds emerge (Fig. 3c).

4. Analyses and discussion

4.1. Particle adsorption at the oil-water interface

A solid particle's affinity for water defines its equilibrium position at the interface. The free energy ΔE associated with the migration of one spherical particle of radius a from the water phase to a planar oil-water interface is a function of the solid-water contact angle θ and the oil-water interfacial tension γ_{ow} ([43], Fig. 4a):

$$\Delta E = -\pi a^2 \gamma_{ow} (1 - \cos\theta)^2 \quad (1)$$

Clearly, completely hydrophobic (θ = 180°) or hydrophilic (θ = 0°) particles prefer to be fully immersed in oil or water, while partially hydrophobic silica nanoparticles take an intermediate position at the interface. Soft particles, such as microgels, experience flattening at the interface because of interfacial tension which could result in higher adsorption energy compared with hard particles [44].

In their initial condition, silica particles are hydrophilic and show no preferential adsorption to the oil–water interface. However, the addition of the surfactant CTAB modifies their wettability and equilibrium position at the interface. Fig. 4b suggests the

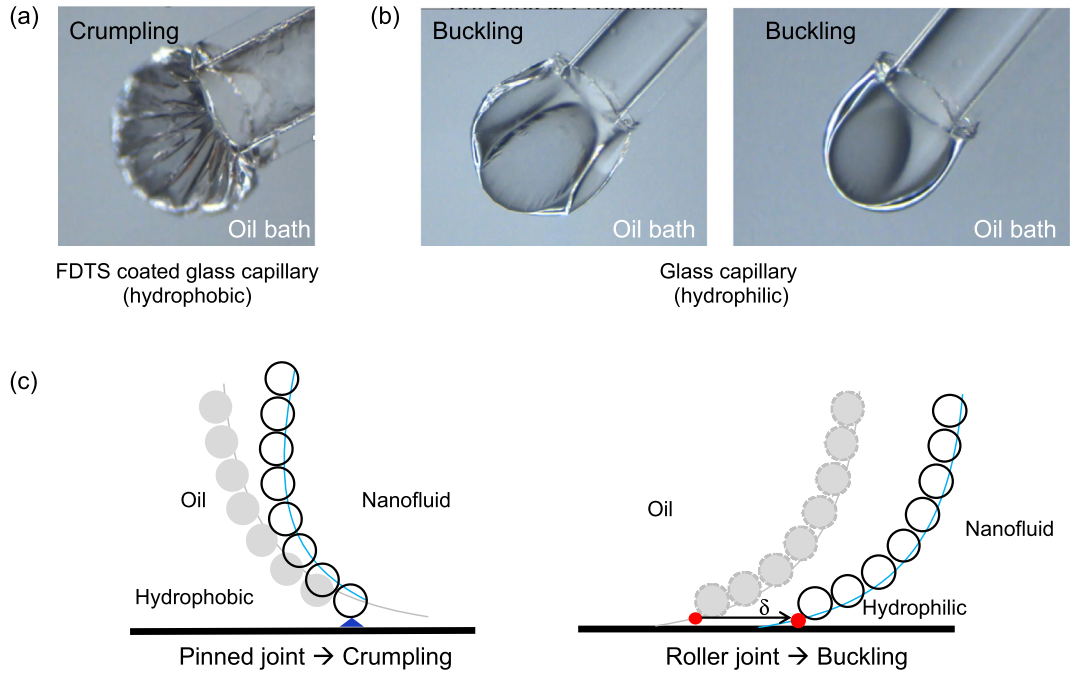

Fig. 3. Pattern formation during droplet contraction: nanofluid droplets in oil. (a) Crumpling pattern. (b) Buckling pattern. (c) Pinned and sliding interactions between the particle-coated interface and the capillary tube.

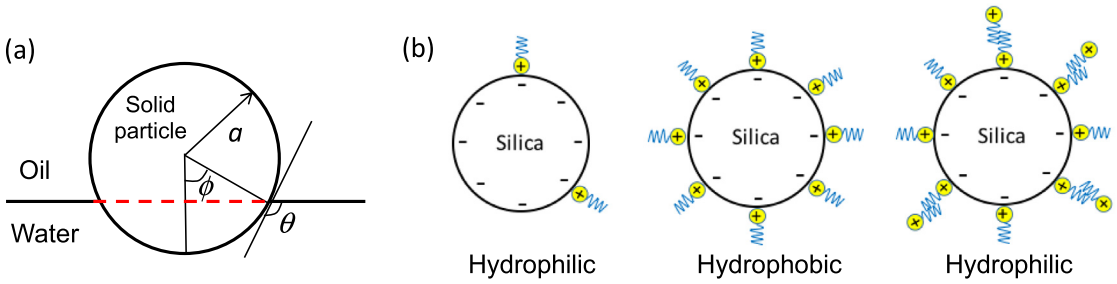

Fig. 4. Particle-level analyses. (a) Particle adsorption at the oil-water interface. (b) Particle-surfactant interactions.

potential interaction between the negatively charged silica nanoparticles and CTAB as a function of the surfactant concentration: CTAB coverage gradually increases until its molecules saturate all sites on the nanoparticle surface. Hydrophobic interactions between carbon chains lead to the adsorption of additional CTAB molecules on the surface, and the formation of micelles at high CTAB concentration. Thus, the wettability of silica particles changes from hydrophilic to hydrophobic with the increase in CTAB concentration, and reverses back to hydrophilic at high concentrations [40]. The intermediate CTAB concentration selected in this study to promote silica nanoparticle adsorption onto the oil-water interface, in agreement with these observations (Fig. 1b).

4.2. Apparent interfacial tension for particle-coated interfaces

The apparent interfacial tension of particle-coated interfaces combines the interfacial tension of the liquid-liquid interface and inter-particle interactions. For simplicity, let us consider an oil-water interface with interfacial tension γ_{ow}. Nanoparticles rest on the interface at an inter-particle distance H and experience an inter-particle repulsive force $F(H)$ which is a function of the particle-particle distance. Particles typically arrange in a hexagonal pattern when dispersed at an interface [45,46], yet, other patterns such as square packing have also been predicted and experimentally observed [47–50]. Consider then the hexagonal and square patterns sketched in Fig. 5. The inter-particle force F is the sum of all particle-particle interactions, which may include electrostatic repulsion, Van der Walls attraction, hydrophobic attraction, and contact force [42,45,51]. The line integral of the tension along the perimeter of the representative area relates the apparent interfacial tension γ_A to the oil-water interfacial tension γ_{ow} and interparticle forces F. The apparent interfacial tension γ_A is:

$$\textit{hexagonal pattern}(\text{Figure 5a}):\gamma_A = \frac{2\sqrt{3}H\gamma_{ow} - 6\cdot F(H)}{2\sqrt{3}H} = \gamma_{ow} - \sqrt{3}\cdot\frac{F(H)}{H} \tag{2a}$$

$$\textit{square pattern}(\text{Figure 5b}):\gamma_A = \frac{4H\gamma_{ow} - 4\cdot F(H)}{4H} = \gamma_{ow} - \frac{F(H)}{H} \tag{2b}$$

In general, the apparent interfacial tension γ_A for nanoparticle coated interfaces is:

$$\gamma_A = \gamma_{ow} - \beta\frac{F(H)}{H} \tag{2c}$$

where β is a packing factor: $\beta = 1$ for square pattern and $\beta = \sqrt{3}$ for hexagonal pattern. Clearly, repulsive particle–particle interactions

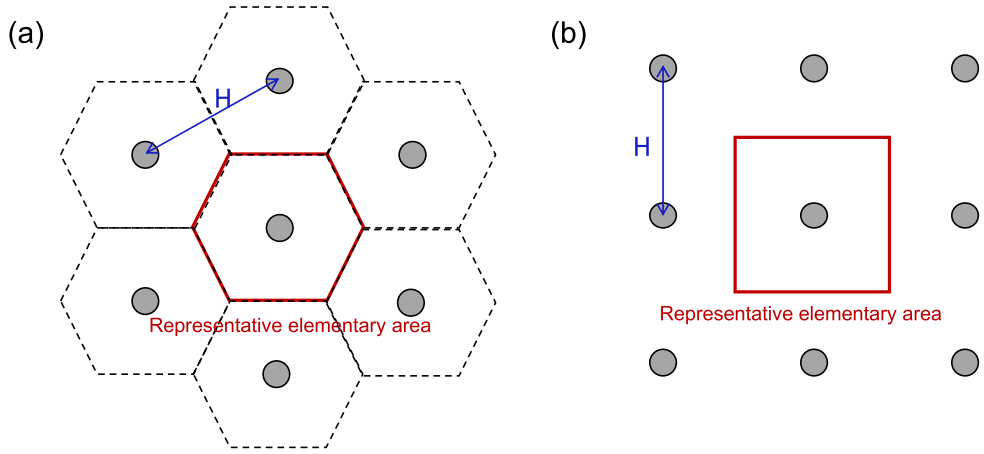

Fig. 5. Apparent interfacial tension of a particle-coated interface. Particles are uniformly distributed with interparticle separation *H*. (a) Hexagonal pattern. (b) Square pattern.

reduce the apparent interfacial tension. The long-range electrostatic repulsion is dominant before particles jam [45]; thereafter, contact force repulsion opposes hydrophobic attraction.

4.3. Particle assembly and re-arrangement during droplet contraction

The particle assembly at the interface evolves in time as particles diffuse from the nanofluid to the interface. Furthermore, an initially loose particle packing at the interface gradually tightens and particles undergo in-plane rearrangement during droplet contraction. Eventually, the granular interface buckles and shears.

Let us assume spherical droplets of radius R, and irreversible particle adsorption to render a surface coverage of particles $c = A_{particle}/A_{interface}$. After a certain adsorption time t_{ad}, the droplet is at the initial state (R_0, c_0) shown as Point 1 in Fig. 2a (Fig. 6a). The interparticle force $F(H)$ is small when the surface coverage is low and the particle–particle distance H is large. As the droplet contracts, particles come closer together and the apparent interfacial tension γ_A gradually decreases (Eq. (2c)). The packing density increases and reaches the jamming condition (R_L, c_L) identified as Point 2 in Fig. 2a (Fig. 6a); repulsive interparticle contact forces reduce the apparent interfacial tension and there is a rapid reduction in capillary pressure.

The granular packing evolves and nanoparticles finally reach a dense packing state (R_D, c_D) identified as Point 3 in Fig. 2a. We assume that the limiting packing density at the onset of buckling corresponds to the hexagonal packing, $c_D = \pi/(2\sqrt{3}) = 0.907$ (last stage in Fig. 6a).

The typical duration of a droplet contraction experiments (time scale in seconds – Fig. 2) is much shorter than the adsorption time

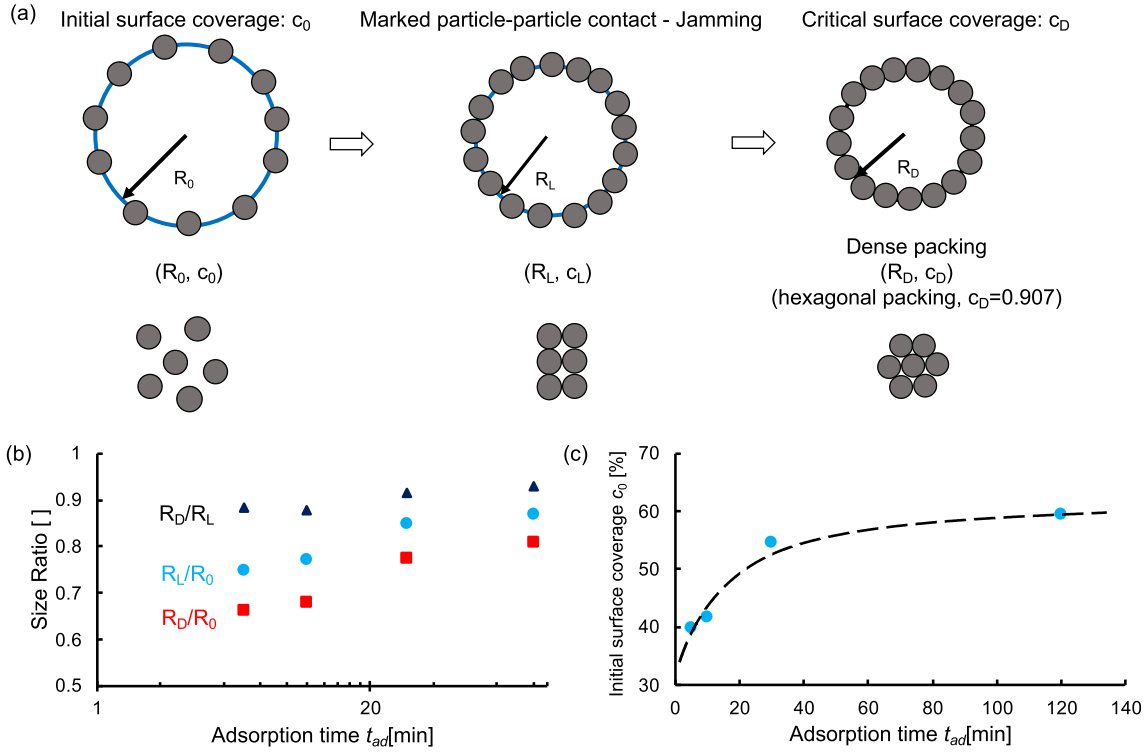

Fig. 6. Particle packing at the interface. (a) Evolution of surface coverage during the contraction of the particle-coated interface. Initial droplet size R_0, droplet radius at the particle jamming R_L, and at the dense packing prior to buckling R_D. (b) Relationship between R_D/R_L, R_L/R_0, and R_D/R_0 and adsorption time t_{ad}. (c) Initial surface coverage c_0 as a function of adsorption time t_{ad}.

t_{ad} (time scale in minutes – Fig. 6). Therefore, the increase in the number of particles at the interface during the test is negligible. Then, let's consider a constant number N_0 of nano-particles of radius a forming a monolayer at the interface. The evolving droplet radius R and the surface concentration c during droplet contraction satisfy the following geometric constraint:

$$4\pi R^2 c = N_0 \pi a^2 \tag{3}$$

Therefore the droplet size ratios are related as (refer to Fig. 6):

$$at \quad jamming: \frac{R_L}{R_0} = \sqrt{\frac{c_0}{c_L}} \tag{4a}$$

$$at \ \ buckling: \frac{R_D}{R_0} = \sqrt{\frac{c_0}{c_D}} \tag{4b}$$

$$\text{and}: \frac{R_D}{R_L} = \sqrt{\frac{c_L}{c_D}} \tag{4c}$$

Fig. 6b shows the experimentally measured ratios R_D/R_0, R_L/R_0, and R_D/R_L for droplets contraction tests run with different adsorption times t_{ad} = 5, 10, 30 and 120 min. The droplet size ratio R_D/R_L is around 0.9 and is independent of the adsorption time. The computed surface coverage at jamming is $c_L \approx 0.73$ (from Eq. (4c)) which is smaller than the coverage for a square packing (c = 0.785); this hints to the role of electrostatic interactions on packing stability.

The size ratios at jamming R_L/R_0 and at the verge of buckling R_D/R_0 increase with adsorption time (Fig. 6b); in other words, the initial surface coverage c_0 increases with adsorption time t_{ad}. Fig. 6c shows the relationship between the initial surface coverage and the adsorption time calculated from the droplet radius R_D at the verge of buckling and the initial droplet size R_0: $c_0 = c_d \cdot R_D^2/R_0^2$ While diffusive transport defines the initial concentration c_0 at time t_{ad} before droplet contraction, the adsorption rate decreases with increasing surface coverage because of steric effects at the interface and the time-decreasing concentration of nanoparticles within the droplet volume [52–54].

4.4. Inter-particle forces

Differences in capillary pressure measured for water-oil droplets (i.e., without interacting particles) and nanofluid-oil droplets (i.e., with interacting particles) reflect the strength of particle interactions (Fig. 2a). The force equilibrium analysis along a droplet equatorial plane relates the interfacial tension γ_{ow} to the capillary pressure $\Delta P = P_{oil}$-P_w (Fig. 7a),

$$\Delta P \pi R^2 = 2\pi R \gamma_{ow} \tag{5}$$

Therefore, the capillary pressure is always positive for an oil droplet in water because of the interfacial tension.

However, experimental result shows that a particle-coated droplet is able to withstand negative capillary pressure $\Delta P = P_{in}$-P_{out} (Fig. 2a and b). An analogous Laplacian-type analysis for a particle-coated droplet $\Delta P \pi R^2 = 2\pi R \gamma_A$ involves the apparent interfacial tension γ_A

(Eq. (2)). For contacting particles (Fig. 7b),

$$hexagonal \ \ pattern\left(\beta = \sqrt{3}, H = 2a\right): \Delta P \pi R^2 = 2\pi R \gamma_{ow} - \frac{\sqrt{3}\pi R}{a} F \tag{6a}$$

$$simple \ \ cubic \ \ pattern(\beta = 1, H = 2a): \Delta P \pi R^2 = 2\pi R \gamma_{ow} - \frac{\pi R}{a} \cdot F \tag{6b}$$

Therefore, the inter-particle force F acting on a nanoparticle is:

$$hexagonal \ \ pattern: F = \frac{\sqrt{3}(2\gamma_{ow} - \Delta P \cdot R)a}{3} \tag{7a}$$

$$square \ \ pattern: F = (2\gamma_{ow} - \Delta P \cdot R)a \tag{7b}$$

The calculated particle-particle contact force ranges from F = 4.9 nN (hexagonal packing) to F = 8.5nN (square packing) for the measured capillary pressure ΔP = -100 Pa (Fig. 2b), droplet size R = 1 mm, nanoparticle radius a = 50 nm, and interfacial tension γ_{ow} = 34.2mN/m (Note: these interparticle contact forces correspond to ~1 MPa in-plane stress for a monolayer thick shell). Clearly, self-organized nanoparticles on the surface of small contracting droplets can sustain higher interparticle forces that those obtained from Langmuir trough experiments [55]. In either case, the strong hydrophobic attraction between the adsorption layers of silica particles contributes to shell stability [55,56].

4.5. Asymmetric behavior

Droplet contraction tests for an "oil droplet in a nanofluid bath" and for a "nanofluid droplet in an oil bath" exhibit distinct shapes and capillary pressure signatures (Fig. 2). This observation indicates an asymmetric nanoparticle-coated interface behavior.

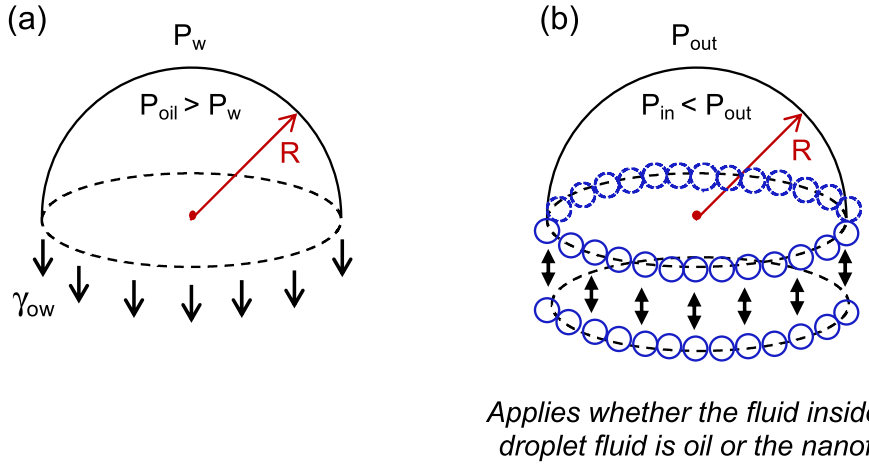

Fig. 7. Equilibrium analyses. (a) An oil droplet in water. (b) A particle-coated droplet.

Consider a particle at a liquid-liquid interface (see optical microscopy images in [21]; freeze-fracture SEM images in [57]; and cyro-SEM images in [8]). Since the buoyant weight is negligible for submicron particles, the relative position of the particle at the interface depends on the contact angle θ. The capillary force F_c that acts on the spherical particle of radius a when it is displaced to a polar angle ϕ with respect to the oil-water interface at equilibrium is (Fig. 8a – see also [58]):

$$F_c(\phi) = 2\pi[a\sin(\theta-\phi)](\gamma_{ow}\sin\phi) \quad (8)$$

Fig. 8b plots the computed capillary force F_c as a function of the polar angle ϕ for various values of the contact angle θ. The capillary force increases when the particle deviates from its equilibrium position and reaches maxima at $\phi = \theta/2$ and $\phi = -(\pi-\theta)/2$.

Let's extend the single particle analysis to a hinged particle arch with an inter-particle angle α (Fig. 8c). The free-body analysis of the intermediate particle 2 shows that the resultant of contact forces F^{12} (the inter-particle force between particles 1 and 2) and F^{23} (between particle 2 and 3) is normal to the arch and is balanced by the capillary force F_c.

$$F_c = \pi a\gamma_{ow}\sin(\theta-\alpha/2) \quad (9)$$

This analysis allows us to compare a particle chain forced to bend towards either the wetting phase (oil – Fig. 8d) or the non-wetting phase (water – Fig. 8e). The interparticle force required to bend the chain towards the wetting phase decreases as the bending angle α increases, and failure happens as soon as bending starts (Fig. 8f). However, when the chain is forced to deform towards the non-wetting phase, the force required to bend the chain increases with the bending angle α, the particle chain is self-stabilizing, and it can sustain a significant out-of-plane loading. The maximum normal force estimated by the particle chain model (F_N = 7.8 nN – Eq. (9)) is consistent with the particle-particle force inferred from measurements (F_N = 4.9 nN-to-8.5 nN – Eq. (7)). Admittedly, other effects such as rolling friction and contact angle hysteresis may play a role but are not considered in this first-order analyses [59–61]. Results from interfacial rheology measurements show that the shear modulus of particle monolayers also depends on the particle wettability [8,62].

The position of the interface relative to the nanoparticles creates a preferential bending direction towards the liquid interface with respect to the interparticle contacts and biases the direction of instabilities: a "nanofluid droplet in an oil bath" develops protruding ridges (Fig. 9a), while an "oil droplet in a nanofluid bath" buckles towards the inside forming invasive crevices (Fig. 9b).

5. Implications: effects on immiscible displacement in porous media

Fluid saturated porous media often experience the invasion of an immiscible fluid. This common phenomenon has important implications to environmental remediation (LNPL's and DNPLs in fresh water aquifers), resource recovery (enhanced oil production) and waste disposal (geological CO_2 storage). Interconnected pores in soils and rocks consist of sequentially converging and diverging cross-sections, thus, fluid interfaces contract and expand as they

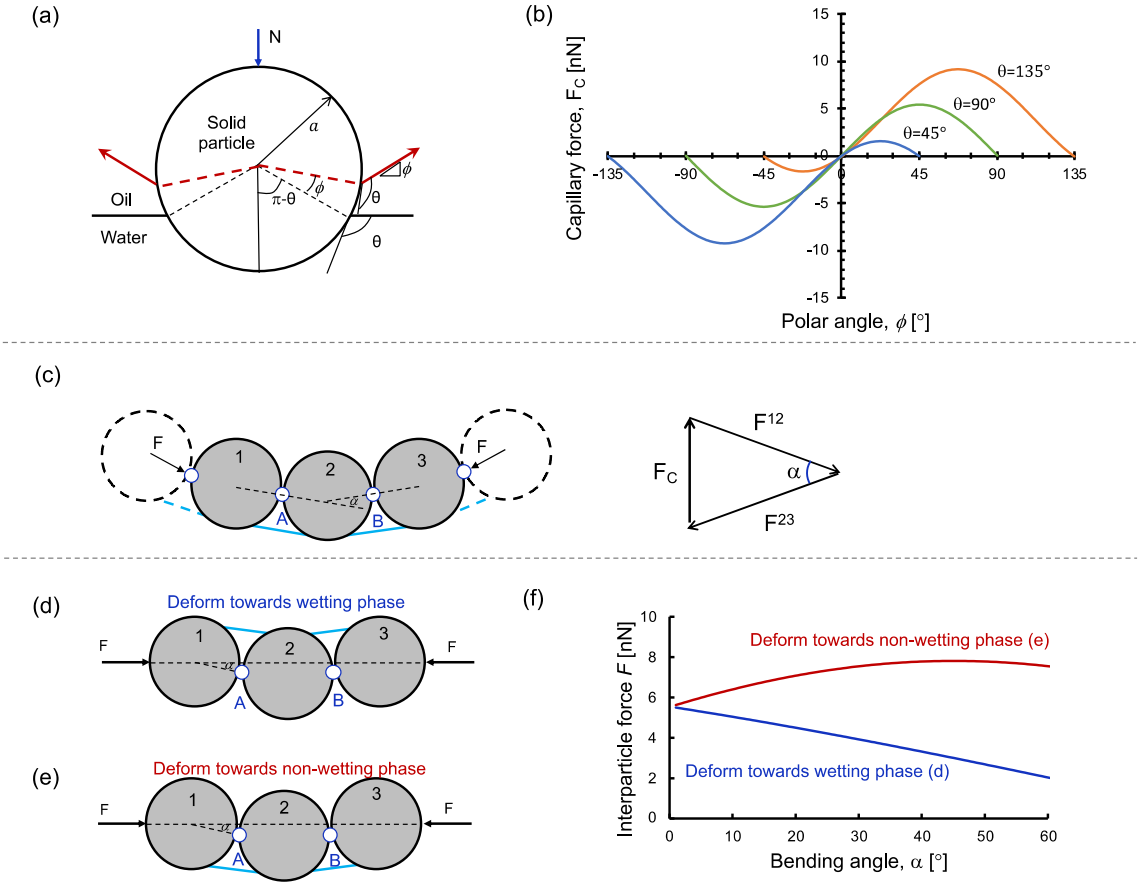

Fig. 8. Asymmetric behavior. (a) A single particle at the oil-water interface. (b) Capillary force as a function of polar angle ϕ for different contact angles θ. Note: particle radius a = 50 nm, oil-water interfacial tension γ_{ow} = 34.2 mN/m. (c) Particle chain and force equilibrium. (d) Buckling of a particle chain towards the wetting phase. (e) Buckling of a particle chain towards the non-wetting phase. (f) The interparticle force F at the bending angle α. Parameters: nanoparticle radius a = 50 nm; oil-water interfacial tensionγ_{ow} = 34.2mN/m; and contact angle θ = 135°.

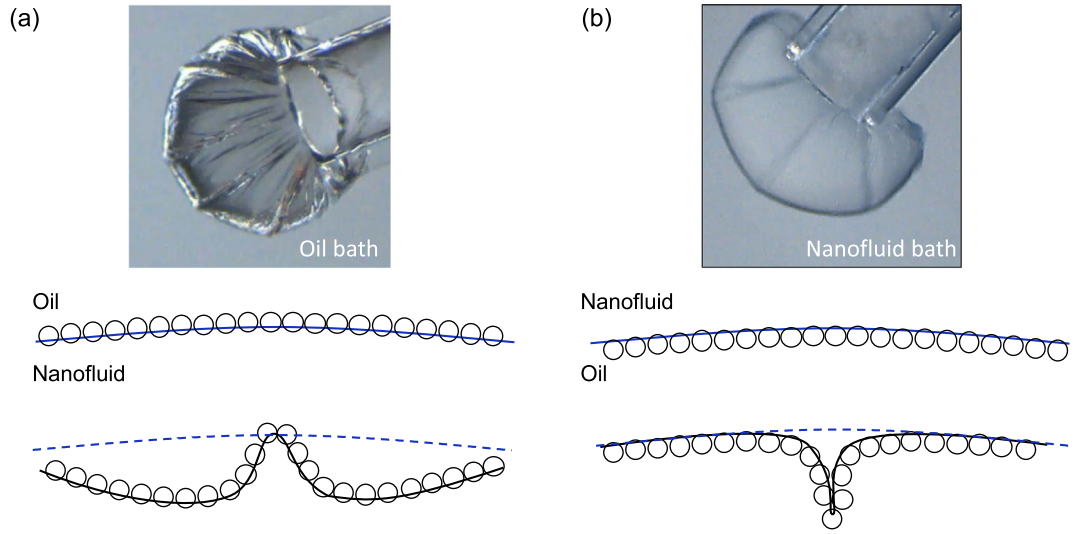

Fig. 9. (fa) Protruding ridges on a nanofluid droplet in an oil bath during contraction. (e) Invasive crevices on an oil droplet in a nanofluid bath during contraction.

traverse the porous medium. Previous studies show that transient changes in surfactant concentration affect the evolution of the capillary pressure across pore constrictions [63]. Similarly, we anticipate that changes in particle concentration can alter the invasion of a particle coated immiscible fluid interface.

A single-constriction experiment illustrates the effect of particle-coated interfaces on the capillary pressure during oil displacement (Fig. 10-a &b – see Supplementary Material V4 for the complete video; for comparison, the capillary pressure evolution for a similar test without nanoparticles is provided in Supplementary Material **S2**). The constricted capillary tube connects to the syringe pump (Braintree Scientific, Inc., BS-8000) and a pressure transducer (PX40, OMEGA) mounted next to the inlet monitors the pressure (see details for a similar setup in [63]). The nanofluid is gradually injected into an oil filled capillary tube. The capillary pressure $\Delta P = P_{oil}$-$P_{nanofluid}$ increases as the interface curvature decreases near the pore constriction and the water-based nanofluid invades the capillary (*Phase A* – before point 1). However, the capillary pressure starts to decrease with increased curvature as the granular shell forms and arches against the pore wall (*Phase B* – points 1 to 4). The shell wrinkles and crumples as it squeezes through the pore throat (points 3 and 4). Then, the interface

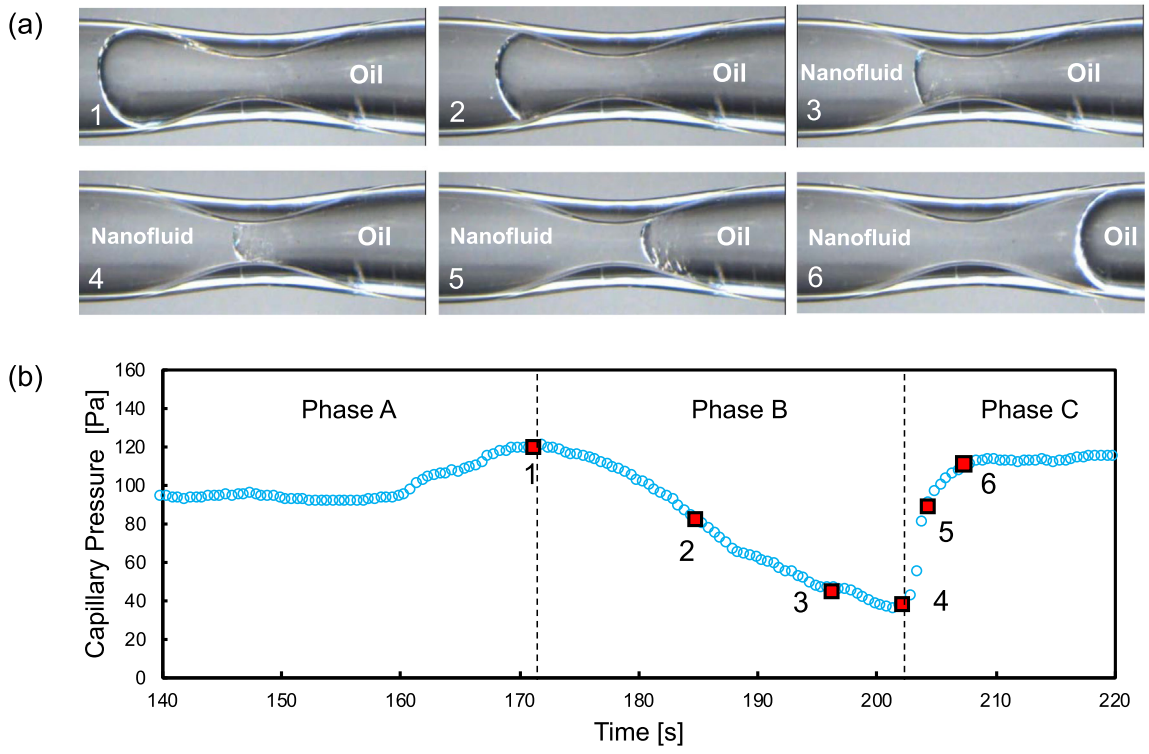

Fig. 10. The influence of a particle-coated interface on oil displacement. (a) A particle-coated interface passes through a pore constriction. (b) The evolution of capillary pressure $\Delta P = P_{oil}$-$P_{nanofluid}$. Note: numbers of markers refer to the sequence of micro photographs. Uncoated borosilicate hydrophilic capillary tube with internal diameter *ID* = 0.97 mm; constriction diameter 0.3 mm.

expands and the capillary pressure recovers after passing the constriction (*Phase C* – points 5 and 6).

The interface expands after constrictions, and particles rearrange by self-assembly. As the interfacial tension homogenizes, the droplet recovers the Laplacian spherical shape (point 4).

Asphaltenes, biofilms and fine particles can adsorb at oil-water or contaminant-water interfaces and may exhibit similar behaviors as the particle-coated interfaces explored in this research [64–67]. Clearly, the formation of particle-coated interfaces during multiphase fluid flow through complex pore networks can have important implications for engineered and natural processes.

6. Conclusions

We investigated the mechanical properties of silica nanoparticle-coated interfaces by analyzing the shapes of interfaces during droplet contraction and expansion, and the associated capillary pressure signature. Our study and analyses emphasize the particulate nature of the modified interface.

Initially, particles diffuse and reach the interface where they self-organize. The interface undergoes a transition from fluid-like to shell-like as the droplet contracts and the self-assembled particles jam at a loose packing configuration. Then, packing evolves to a dense configuration before the particle-coated interface buckles. Particle-particle interactions result in a reduced apparent interfacial tension for the particle-coated interface. In fact, the apparent interfacial tension may become negative, as well as the capillary pressure.

Previous work observed various buckling patterns when particle-coated interfaces were compressed and suggested that the elastoplastic characteristics of the thin film determined the deformed topology [15,35,68]. Here, we show that the buckling patterns also depend on the interaction between the particle-coated interface and the solid boundary. Constrained displacement (“pinned joints”) leads to crumpling patterns, while free displacement (“roller joints”) results in a few buckles.

Furthermore, results demonstrate that particle-coated interfaces exhibit asymmetric mechanical behavior. The “nanofluid droplet in an oil bath” buckles at a negligible pressure difference $\Delta P \rightarrow 0$ in agreement with previous work [34], while an “oil droplet in a nanofluid bath” withstands a significant pressure difference. A particle-level analysis shows that the liquid-liquid interface contributes a larger restoring force when the particle chain bends towards the non-wetting phase. This asymmetric mechanical behavior creates a preferential bending direction and biases the direction of instabilities.

Our experimental results also show that the contraction and expansion of particle-coated interfaces affect multiphase displacement in converging-diverging pores. This pore-scale phenomenon remained undetected in previous core-flooding experiments and pore-scale observations [3,69]. In particular, we show that the formation of the granular shell-like interface hinders the increase in capillary pressure during the invasion of wetting fluids across pore constrictions. Therefore, the presence of nanoparticles at fluid interfaces alters mixed fluid displacement in porous media. This interfacial phenomenon may have significant implications for environmental remediation, oil recovery and CO_2 injection.

Declaration of Competing Interest

The authors declare that they have no known competing financial interests or personal relationships that could have appeared to influence the work reported in this paper.

Acknowledgments

Support for this research was provided by the KAUST endowment. G. Abelskamp edited the manuscript. We are grateful to the anonymous reviewers for their detailed reviews and insightful observations.

Appendix A. Supplementary data

Supplementary data to this article can be found online at https://doi.org/10.1016/j.jcis.2020.07.110.

References

[1] B.P. Binks, Particles as surfactants – similarities and differences, Curr. Opin. Colloid Interface Sci. 7 (2002) 21–41, https://doi.org/10.1016/S1359-0294(02)00008-0.
[2] Y. Chevalier, M.A. Bolzinger, Emulsions stabilized with solid nanoparticles: pickering emulsions, Colloids Surfaces A Physicochem. Eng. Asp. 439 (2013) 23–34, https://doi.org/10.1016/j.colsurfa.2013.02.054.
[3] D. Luo, F. Wang, J. Zhu, F. Cao, Y. Liu, X. Li, R.C. Willson, Z. Yang, C.W. Chu, Z. Ren, Nanofluid of graphene-based amphiphilic Janus nanosheets for tertiary or enhanced oil recovery: high performance at low concentration, Proc. Natl. Acad. Sci. U.S.A. 113 (2016) 7711–7716, https://doi.org/10.1073/pnas.1608135113.
[4] J. Frelichowska, M.A. Bolzinger, J.P. Valour, H. Mouaziz, J. Pelletier, Y. Chevalier, Pickering w/o emulsions: drug release and topical delivery, Int. J. Pharm. 368 (2009) 7–15, https://doi.org/10.1016/j.ijpharm.2008.09.057.
[5] D.N. Espinoza, J.C. Santamarina, Water-CO2-mineral systems: interfacial tension, contact angle, and diffusionImplications to CO2 geological storage, Water Resour. Res. 46 (2010) 7537, https://doi.org/10.1029/2009WR008634.
[6] D.Y. Zang, E. Rio, D. Langevin, B. Wei, B.P. Binks, Viscoelastic properties of silica nanoparticle monolayers at the air-water interface, Eur. Phys. J. E. 31 (2010) 125–134, https://doi.org/10.1140/epje/i2010-10565-7.
[7] A.J. Mendoza, E. Guzmán, F. Martínez-Pedrero, H. Ritacco, R.G. Rubio, F. Ortega, V.M. Starov, R. Miller, Particle laden fluid interfaces: dynamics and interfacial rheology, Adv. Colloid Interface Sci. 206 (2014) 303–319, https://doi.org/10.1016/j.cis.2013.10.010.
[8] O.S. Deshmukh, D. Van Den Ende, M.C. Stuart, F. Mugele, M.H.G. Duits, Hard and soft colloids at fluid interfaces: adsorption, interactions, assembly & rheology, Adv. Colloid Interface Sci. 222 (2015) 215–227, https://doi.org/10.1016/j.cis.2014.09.003.
[9] D. Vella, P. Aussillous, L. Mahadevan, Elasticity of an interfacial particle raft, Europhys. Lett. 68 (2004) 212–218, https://doi.org/10.1209/epl/i2004-10202-x.
[10] L. Pocivavsek, S.L. Frey, K. Krishan, K. Gavrilov, P. Ruchala, A.J. Waring, F.J. Walther, M. Dennin, T.A. Witten, K.Y.C. Lee, Lateral stress relaxation and collapse in lipid monolayers, Soft Matter 4 (2008) 2019–2029, https://doi.org/10.1039/b804611e.
[11] P. Cicuta, E.J. Stancik, G.G. Fuller, Shearing or compressing a soft glass in 2D: time-concentration superposition, Phys. Rev. Lett. 90 (2003) 4, https://doi.org/10.1103/PhysRevLett.90.236101.
[12] B.D. Leahy, L. Pocivavsek, M. Meron, K.L. Lam, D. Salas, P.J. Viccaro, K.Y.C. Lee, B. Lin, Geometric stability and elastic response of a supported nanoparticle film, Phys. Rev. Lett. 105 (2010) 58301, https://doi.org/10.1103/PhysRevLett.105.058301.
[13] S. Dasgupta, T. Auth, G. Gompper, Nano- and microparticles at fluid and biological interfaces, J. Phys. Condens. Matter. 29 (2017), https://doi.org/10.1088/1361-648X/aa7933 373003.
[14] F. Bresme, M. Oettel, Nanoparticles at fluid interfaces, J. Phys. Condens. Matter. 19 (2007), https://doi.org/10.1088/0953-8984/19/41/413101 413101.
[15] E. Jambon-Puillet, C. Josserand, S. Protière, Wrinkles, folds, and plasticity in granular rafts, Phys. Rev. Mater. 1 (2017) 42601, https://doi.org/10.1103/PhysRevMaterials.1.042601.
[16] S. Razavi, K.D. Cao, B. Lin, K.Y.C. Lee, R.S. Tu, I. Kretzschmar, Collapse of particle-laden interfaces under compression: buckling vs particle expulsion, Langmuir 31 (2015) 7764–7775, https://doi.org/10.1021/acs.langmuir.5b01652.
[17] V. Garbin, Collapse mechanisms and extreme deformation of particle-laden interfaces, Curr. Opin. Colloid Interface Sci. 39 (2019) 202–211, https://doi.org/10.1016/j.cocis.2019.02.007.
[18] C. Gu, L. Botto, Buckling: vs. particle desorption in a particle-covered drop subject to compressive surface stresses: a simulation study, Soft Matter 14 (2018) 711–724, https://doi.org/10.1039/c7sm01912b.
[19] K.H. Kim, B.Q. Kim, J.Q. Kim, S.Q. Choi, New collapse mechanism of colloidal particle monolayers via depletion pressure: formation of large-area particle multilayers at the air-water interface, J. Phys. Chem. C (2019), https://doi.org/10.1021/acs.jpcc.9b06963.
[20] E. Santini, J. Krägel, F. Ravera, L. Liggieri, R. Miller, Study of the monolayer structure and wettability properties of silica nanoparticles and CTAB using the

Langmuir trough technique, Colloids Surfaces A Physicochem. Eng. Asp. 382 (2011) 186–191, https://doi.org/10.1016/j.colsurfa.2010.11.042.
[21] A. Deák, E. Hild, A.L. Kovács, Z. Hórvölgyi, Contact angle determination of nanoparticles: film balance and scanning angle reflectometry studies, Phys. Chem. Chem. Phys. 9 (2007) 6359–6370, https://doi.org/10.1039/b702937n.
[22] T.S. Horozov, B.P. Binks, R. Aveyard, J.H. Clint, Effect of particle hydrophobicity on the formation and collapse of fumed silica particle monolayers at the oil-water interface, Colloids Surfaces A Physicochem. Eng. Asp. 282–283 (2006) 377–386, https://doi.org/10.1016/j.colsurfa.2005.11.085.
[23] P. Cicuta, D. Vella, Granular character of particle rafts, Phys. Rev. Lett. 102 (2009), https://doi.org/10.1103/PhysRevLett.102.138302 138302.
[24] E. Aumaitre, D. Vella, P. Cicuta, On the measurement of the surface pressure in Langmuir films with finite shear elasticity, Soft Matter 7 (2011) 2530–2537, https://doi.org/10.1039/c0sm01213k.
[25] I. Chatzis, F.A.L. Dullien, Dynamic immiscible displacement mechanisms in pore doublets: theory versus experiment, J. Colloid Interface Sci. 91 (1983) 199–222, https://doi.org/10.1016/0021-9797(83)90326-0.
[26] M.J. Blunt, Flow in porous media – pore-network models and multiphase flow, Curr. Opin. Colloid Interface Sci. 6 (2001) 197–207, https://doi.org/10.1016/S1359-0294(01)00084-X.
[27] W.G. Gray, S.M. Hassanizadeh, Unsaturated flow theory including interfacial phenomena, Water Resour. Res. 27 (1991) 1855–1863, https://doi.org/10.1029/91WR01260.
[28] J.C. Santamarina, Z. Sun, Mixed fluid conditions: capillary phenomena, in: PoromechanicsVI, American Society of Civil Engineers, Reston, VA, 2017, pp. 70–89. 10.1061/9780784480779.010.
[29] Z. Sun, J.C. Santamarina, Haines jumps: pore scale mechanisms, Phys. Rev. E 100 (2019), https://doi.org/10.1103/PhysRevE.100.023115.
[30] S. Berg, H. Ott, S.A. Klapp, A. Schwing, R. Neiteler, N. Brussee, A. Makurat, L. Leu, F. Enzmann, J.-O. Schwarz, M. Kersten, S. Irvine, M. Stampanoni, Real-time 3D imaging of Haines jumps in porous media flow, Proc. Natl. Acad. Sci. 110 (10) (2013) 3755–3759, https://doi.org/10.1073/pnas.1221373110.
[31] W.R. Rossen, A critical review of Roof snap-off as a mechanism of steady-state foam generation in homogeneous porous media, Colloids Surfaces A Physicochem. Eng. Asp. 225 (2003) 1–24, https://doi.org/10.1016/S0927-7757(03)00309-1.
[32] A.R. Kovscek, G.Q. Tang, C.J. Radke, Verification of Roof snap off as a foam-generation mechanism in porous media at steady state, Colloids Surfaces A Physicochem. Eng. Asp. 302 (2007) 251–260, https://doi.org/10.1016/j.colsurfa.2007.02.035.
[33] S.O. Asekomhe, R. Chiang, J.H. Masliyah, J.A.W. Elliott, Some observations on the contraction behavior of a water-in-oil drop with attached solids, Ind. Eng. Chem. Res. 44 (2005) 1241–1249, https://doi.org/10.1021/ie040134b.
[34] C. Monteux, J. Kirkwood, H. Xu, E. Jung, G.G. Fuller, Determining the mechanical response of particle-laden fluid interfaces using surface pressure isotherms and bulk pressure measurements of droplets, Phys. Chem. Chem. Phys. 9 (2007) 6344–6350, https://doi.org/10.1039/b708962g.
[35] S.S. Datta, H.C. Shum, D.A. Weitz, Controlled buckling and crumpling of nanoparticle-coated droplets, Langmuir 26 (2010) 18612–18616, https://doi.org/10.1021/la103874z.
[36] N.J. Alvarez, S.L. Anna, T. Saigal, R.D. Tilton, L.M. Walker, Interfacial dynamics and rheology of polymer-grafted nanoparticles at air-water and xylene-water interfaces, Langmuir 28 (2012) 8052–8063, https://doi.org/10.1021/la300737p.
[37] N.J. Alvarez, L.M. Walker, S.L. Anna, A microtensiometer to probe the effect of radius of curvature on surfactant transport to a spherical interface, Langmuir 26 (2010) 13310–13319, https://doi.org/10.1021/la101870m.
[38] L. Liggieri, F. Ravera, A. Passerone, Drop formation instabilities induced by entrapped gas bubbles, J. Colloid Interface Sci. 140 (1990) 436–443, https://doi.org/10.1016/0021-9797(90)90364-T.
[39] A. Passerone, L. Liggieri, F. Ravera, Growth instabilities of bubbles and drops, Springer, Berlin, Heidelberg, 1991, pp. 268–272. 10.1007/3-540-54367-8_57.
[40] A. Maestro, E. Guzmán, E. Santini, F. Ravera, L. Liggieri, F. Ortega, R.G. Rubio, Wettability of silica nanoparticle-surfactant nanocomposite interfacial layers, Soft Matter 8 (2012) 837–843, https://doi.org/10.1039/c1sm06421e.
[41] F. Ravera, E. Santini, G. Loglio, M. Ferrari, L. Liggieri, Effect of nanoparticles on the interfacial properties of liquid/liquid and liquid/air surface layers, J. Phys. Chem. B. 110 (2006) 19543–19551, https://doi.org/10.1021/jp0636468.
[42] E.E. Meyer, K.J. Rosenberg, J. Israelachvili, Recent progress in understanding hydrophobic interactions, Proc. Natl. Acad. Sci. 103 (2006) 15739–15746.
[43] S. Levine, B.D. Bowen, S.J. Partridge, Stabilization of emulsions by fine particles II. Capillary and van der Waals forces between particles, Colloids Surf. 38 (1989) 345–364, https://doi.org/10.1016/0166-6622(89)80272-0.
[44] F. Camerin, M.Á. Fernández-Rodríguez, L. Rovigatti, M.N. Antonopoulou, N. Gnan, A. Ninarello, L. Isa, E. Zaccarelli, Microgels adsorbed at liquid-liquid interfaces: a joint numerical and experimental study, ACS Nano 13 (2019) 4548–4559, https://doi.org/10.1021/acsnano.9b00390.
[45] R. Aveyard, J.H. Clint, D. Nees, V.N. Paunov, Compression and structure of monolayers of charged latex particles at air/water and octane/water interfaces, Langmuir 16 (2000) 1969–1979, https://doi.org/10.1021/la990887g.
[46] T.S. Horozov, R. Aveyard, J.H. Clint, B.P. Binks, Order-disorder transition in monolayers of modified monodisperse silica particles at the octane-water interface, Langmuir 19 (2003) 2822–2829, https://doi.org/10.1021/la020858x.
[47] E.A. Jagla, Minimum energy configurations of repelling particles in two dimensions, J. Chem. Phys. 110 (1999) 451–456, https://doi.org/10.1063/1.478105.
[48] M. Rey, A.D. Law, D.M.A. Buzza, N. Vogel, Anisotropic self-assembly from isotropic colloidal building blocks, J. Am. Chem. Soc. 139 (2017) 17464–17473, https://doi.org/10.1021/jacs.7b08503.
[49] M. Rey, T. Yu, K. Bley, K. Landfester, D.M.A. Buzza, N. Vogel, Amphiphile-induced anisotropic colloidal self-assembly, Langmuir 34 (2018) 9990–10000, https://doi.org/10.1021/acs.langmuir.8b01382.
[50] W.R.C. Somerville, A.D. Law, M. Rey, N. Vogel, A.J. Archer, D.M.A. Buzza, Pattern formation in two-dimensional hard-core/soft-shell systems with variable soft shell profiles, Soft Matter 16 (2020) 3564–3573, https://doi.org/10.1039/d0sm00092b.
[51] J.N. Israelachvili, Intermolecular and Surface Forces: Third Edition, 2011. https://doi.org/10.1016/C2011-0-05119-0.
[52] A.F.H. Ward, L. Tordai, Time-dependence of boundary tensions of solutions I. The role of diffusion in time-effects, J. Chem. Phys. 14 (1946) 453–461, https://doi.org/10.1063/1.1724167.
[53] S. Kutuzov, J. He, R. Tangirala, T. Emrick, T.P. Russell, A. Böker, On the kinetics of nanoparticle self-assembly at liquid/liquid interfaces, Phys. Chem. Chem. Phys. 9 (2007) 6351–6358, https://doi.org/10.1039/b710060b.
[54] S. Kutuzov, J. He, R. Tangirala, T. Emrick, T.P. Russell, A. Boker, On the kinetics of nanoparticle self-assembly at liquid/liquid interfaces, Phys. Chem. Chem. Phys. 9 (2007) 6313–6318, https://doi.org/10.1039/b705094a.
[55] C.E. McNamee, M. Kappl, Forces and physical properties of the Langmuir monolayers of TiO2 particles at air/water interfaces after collisions by a particle in water, RSC Adv. 6 (2016) 54440–54448, https://doi.org/10.1039/c6ra09499f.
[56] A.G. Bykov, B.A. Noskov, G. Loglio, V.V. Lyadinskaya, R. Miller, Dilational surface elasticity of spread monolayers of polystyrene microparticles, Soft Matter 10 (2014) 6499–6505, https://doi.org/10.1039/c4sm00782d.
[57] A.B. Subramaniam, M. Abkarian, L. Mahadevan, H.A. Stone, Mechanics of interfacial composite materials, Langmuir 22 (2006) 10204–10208, https://doi.org/10.1021/la061475s.
[58] A.V. Rapacchietta, A.W. Neumann, Force and free-energy analyses of small particles at fluid interfaces. II. Spheres, J. Colloid Interface Sci. 59 (1977) 555–567, https://doi.org/10.1016/0021-9797(77)90051-0.
[59] L.O. Heim, J. Blum, M. Preuss, H.J. Butt, Adhesion and friction forces between spherical micrometer-sized particles, Phys. Rev. Lett. 83 (1999) 3328–3331, https://doi.org/10.1103/PhysRevLett.83.3328.
[60] C. Dominik, A.G.G.M. Tielens, Resistance to rolling in the adhesive contact of two elastic spheres, Philos. Mag. A Phys. Condens. Matter, Struct. Defects Mech. Prop. 72 (1995) 783–803, https://doi.org/10.1080/01418619508243800.
[61] W.J. Lokar, W.A. Ducker, Proximal adsorption at glass surfaces: ionic strength, pH, chain length effects, Langmuir 20 (2004) 378–388, https://doi.org/10.1021/la035288v.
[62] D.Y. Zang, E. Rio, G. Delon, D. Langevin, B. Wei, B.P. Binks, Influence of the contact angle of silica nanoparticles at the air-water interface on the mechanical properties of the layers composed of these particles, Mol. Phys. 109 (2011) 1057–1066, https://doi.org/10.1080/00268976.2010.542778.
[63] J. Jang, Z. Sun, J.C. Santamarina, Capillary pressure across a pore throat in the presence of surfactants, Water Resour. Res. 52 (2016) 9586–9599, https://doi.org/10.1002/2015WR018499.
[64] S. Gao, K. Moran, Z. Xu, J. Masliyah, Role of bitumen components in stabilizing water-in-diluted oil emulsions, Energy Fuels 23 (2009) 2606–2612, https://doi.org/10.1021/ef801089c.
[65] J.K. Kim, P.A. Rühs, P. Fischer, J.S. Hong, Interfacial localization of nanoclay particles in oil-in-water emulsions and its reflection in interfacial moduli, Rheol. Acta. 52 (2013) 327–335, https://doi.org/10.1007/s00397-013-0689-3.
[66] P.A. Rühs, L. Böni, G.G. Fuller, R.F. Inglis, P. Fischer, In-situ quantification of the interfacial rheological response of bacterial biofilms to environmental stimuli, PLoS ONE 8 (2013), https://doi.org/10.1371/journal.pone.0078524 e78524.
[67] Z. Kang, A. Yeung, J.M. Foght, M.R. Gray, Mechanical properties of hexadecane-water interfaces with adsorbed hydrophobic bacteria, Colloids Surfaces B Biointerfaces 62 (2008) 273–279, https://doi.org/10.1016/j.colsurfb.2007.10.021.
[68] T.D. Kassuga, J.P. Rothstein, The effect of shear and confinement on the buckling of particle-laden interfaces, J. Phys. Condens. Matter. 28 (2016), https://doi.org/10.1088/0953-8984/28/2/025101.
[69] M. Zargartalebi, R. Kharrat, N. Barati, Enhancement of surfactant flooding performance by the use of silica nanoparticles, Fuel 143 (2015) 21–27, https://doi.org/10.1016/j.fuel.2014.11.040.